

Method for auto-alignment of digital optical phase conjugation systems based on digital propagation

Mooseok Jang,^{1,2,*} Haowen Ruan,^{1,2} Haojiang Zhou,¹ Benjamin Judkewitz,¹ and Changhui Yang¹

¹Electrical Engineering, California Institute of Technology, 1200 East California Boulevard, Pasadena, California 91125, USA

²These authors contributed equally to this paper
^{*}mjang@caltech.edu

Abstract: Optical phase conjugation (OPC) has enabled many optical applications such as aberration correction and image transmission through fiber. In recent years, implementation of digital optical phase conjugation (DOPC) has opened up the possibility of its use in biomedical optics (e.g. deep-tissue optical focusing) due to its ability to provide greater-than-unity OPC reflectivity (the power ratio of the phase conjugated beam and input beam to the OPC system) and its flexibility to accommodate additional wavefront manipulations. However, the requirement for precise (pixel-to-pixel matching) alignment of the wavefront sensor and the spatial light modulator (SLM) limits the practical usability of DOPC systems. Here, we report a method for auto-alignment of a DOPC system by which the misalignment between the sensor and the SLM is auto-corrected through digital light propagation. With this method, we were able to accomplish OPC playback with a DOPC system with gross sensor-SLM misalignment by an axial displacement of up to $\sim 1.5\text{ cm}$, rotation and tip/tilt of $\sim 5^\circ$, and in-plane displacement of $\sim 5\text{ mm}$ (dependent on the physical size of the sensor and the SLM). Our auto-alignment method robustly achieved a DOPC playback peak-to-background ratio (PBR) corresponding to more than $\sim 30\%$ of the theoretical maximum. As an additional advantage, the auto-alignment procedure can be easily performed at will and, as such, allows us to correct for small mechanical drifts within the DOPC systems, thus overcoming a previously major DOPC system vulnerability. We believe that this reported method for implementing robust DOPC systems will broaden the practical utility of DOPC systems.

©2014 Optical Society of America

OCIS codes: (070.5040) Phase conjugation; (070.7345) Wave propagation; (090.1995) Digital holography; (090.2880) Holographic interferometry; (110.7050) Turbid media; (220.1080) Active or adaptive optics.

References and links

1. A. Yariv, "Phase Conjugate Optics and Real-Time Holography," *IEEE J Quantum Electron.* **14**(9), 650–660 (1978).
2. R. Hellwarth, "Generation of time-reversed wave fronts by nonlinear refraction," *JOSA* **90007**, 1976–1978 (1977).
3. V. Wang and C. R. Giuliano, "Correction of phase aberrations via stimulated Brillouin scattering," *Opt. Lett.* **2**(1), 4–6 (1978).
4. R. C. Lind and D. G. Steel, "Demonstration of the longitudinal modes and aberration correction properties of a continuous-wave dye laser with a phase-conjugate mirror," *Opt. Lett.* **6**(11), 554–556 (1981).

5. D. M. Pepper, D. Fekete, and A. Yariv, "Observation of amplified phase-conjugate reflection and optical parametric oscillation by degenerate four-wave mixing in a transparent medium," *Appl. Phys. Lett.* **33**(1), 41 (1978).
6. J. Auyeung, D. Fekete, D. M. Pepper, and A. Yariv, "A theoretical and experimental investigation of the modes of optical resonators with phase-conjugate mirrors," *IEEE J Quantum Electron.* **15**(10), 1180–1188 (1979).
7. A. Yariv, D. Fekete, and D. M. Pepper, "Compensation for channel dispersion by nonlinear optical phase conjugation," *Opt. Lett.* **4**(2), 52 (1979).
8. M. C. Gower and R. G. Caro, "KrF laser with a phase-conjugate Brillouin mirror," *Opt. Lett.* **7**(4), 162–164 (1982).
9. G. J. Dunning and R. C. Lind, "Demonstration of image transmission through fibers by optical phase conjugation," *Opt. Lett.* **7**(11), 558–560 (1982).
10. D. M. Bloom and G. C. Bjorklund, "Conjugate wave-front generation and image reconstruction by four-wave mixing," *Appl. Phys. Lett.* **31**(9), 592 (1977).
11. M. D. Levenson, "High-resolution imaging by wave-front conjugation," *Opt. Lett.* **5**(5), 182 (1980).
12. Z. Yaqoob, D. Psaltis, M. S. Feld, and C. Yang, "Optical Phase Conjugation for Turbidity Suppression in Biological Samples," *Nat. Photonics* **2**(2), 110–115 (2008).
13. E. J. McDowell, M. Cui, I. M. Vellekoop, V. Senekerimyan, Z. Yaqoob, and C. Yang, "Turbidity suppression from the ballistic to the diffusive regime in biological tissues using optical phase conjugation," *J. Biomed. Opt.* **15**(2), 025004 (2010).
14. X. Xu, H. Liu, and L. V. Wang, "Time-reversed ultrasonically encoded optical focusing into scattering media," *Nat. Photonics* **5**(3), 154–157 (2011).
15. Y. M. Wang, B. Judkewitz, C. A. Dimarzio, and C. Yang, "Deep-tissue focal fluorescence imaging with digitally time-reversed ultrasound-encoded light," *Nat Commun* **3**, 928 (2012).
16. C. L. Hsieh, Y. Pu, R. Grange, and D. Psaltis, "Digital phase conjugation of second harmonic radiation emitted by nanoparticles in turbid media," *Opt. Express* **18**(12), 12283–12290 (2010).
17. I. M. Vellekoop, M. Cui, and C. Yang, "Digital optical phase conjugation of fluorescence in turbid tissue," *Appl. Phys. Lett.* **101**(8), 081108 (2012).
18. M. Jang, A. Sentenac, and C. Yang, "Optical phase conjugation (OPC)-assisted isotropic focusing," *Opt. Express* **21**(7), 8781–8792 (2013).
19. B. Zel'Dovich, V. Popovichev, V. Ragul'skii, and F. Faizullov, "Connection between the wave fronts of the reflected and exciting light in stimulated Mandel'shtam-Brillouin scattering," *J. Exp. Theor. Phys.* **15**, 109–112 (1972).
20. M. Gower and D. Proch, *Optical Phase Conjugation* (Springer, 1994).
21. Y. Suzuki, P. Lai, X. Xu, and L. Wang, "High-sensitivity ultrasound-modulated optical tomography with a photorefractive polymer," *Opt. Lett.* **38**(6), 899–901 (2013).
22. B. Judkewitz, Y. M. Wang, R. Horstmeyer, A. Mathy, and C. Yang, "Speckle-scale focusing in the diffusive regime with time-reversal of variance-encoded light (TROVE)," *Nat. Photonics* **7**(4), 300–305 (2013).
23. M. Cui and C. Yang, "Implementation of a digital optical phase conjugation system and its application to study the robustness of turbidity suppression by phase conjugation," *Opt. Express* **18**(4), 3444–3455 (2010).
24. C. Bellanger, A. Brignon, J. Colineau, and J. P. Huignard, "Coherent fiber combining by digital holography," *Opt. Lett.* **33**(24), 2937–2939 (2008).
25. I. Yamaguchi and T. Zhang, "Phase-shifting digital holography," *Opt. Lett.* **22**(16), 1268–1270 (1997).
26. I. M. Vellekoop and A. P. Mosk, "Focusing coherent light through opaque strongly scattering media," *Opt. Lett.* **32**(16), 2309–2311 (2007).
27. S. M. Popoff, G. Lerosey, R. Carminati, M. Fink, A. C. Boccara, and S. Gigan, "Measuring the Transmission Matrix in Optics: An Approach to the Study and Control of Light Propagation in Disordered Media," *Phys. Rev. Lett.* **104**(10), 100601 (2010).
28. J. Goodman, *Introduction to Fourier Optics* (Roberts and Company Publishers, 2005).
29. J. Li, Z. Peng, and Y. Fu, "Diffraction transfer function and its calculation of classic diffraction formula," *Opt. Commun.* **280**(2), 243–248 (2007).
30. K. Matsushima, H. Schimmel, and F. Wyrowski, "Fast calculation method for optical diffraction on tilted planes by use of the angular spectrum of plane waves," *J. Opt. Soc. Am. A* **20**(9), 1755–1762 (2003).
31. S. Feng, C. Kane, P. A. Lee, and A. D. Stone, "Correlations and fluctuations of coherent wave transmission through disordered media," *Phys. Rev. Lett.* **61**(7), 834–837 (1988).

1. Introduction

Optical phase conjugation is an optical process by which a phase-conjugated light wave can be made to retrace the original light wave in the backward direction (time-reversal property). Because of this property, OPC has been of interest in many optical applications including aberration correction [1–4], optical resonators [5,6], pulse compression [7,8], image transmission through fibers [1,9], and high-resolution imaging [10,11] for more than 40 years.

In the field of biomedical optics, some significant breakthroughs have recently been made by capitalizing on the time-reversal property of optical phase conjugation to tackle optical

scattering [12]. reported the first experimental demonstration of OPC-based cancellation of optical scattering inside a biological tissue section. In that study, optical focusing was achieved through a 0.69 mm -thick chicken breast tissue in which photons were scattered ~ 25 times on average. A follow-up study demonstrated successful focusing through up to 7 mm of chicken breast tissue [13]. Subsequently [14], and [15] reported the successful application of OPC in combination with ultrasound tagging to render optical focusing in a prior unattained tissue depth. This class of methods is termed time-reversed ultrasonically encoded (TRUE) optical focusing. OPC-assisted deep tissue optical focusing has also been demonstrated with a second harmonic generation (SHG) active nanomaterial and with fluorescence beads (with a narrow band-width filter) [16,17]. Ultrasound wave, SHG active material, and fluorescent bead with a filter all serve as localized coherent light sources inside tissue media that can be time-reversed by the OPC process. The symmetric optical propagation property of OPC further enables the generation of a quasi-isotropic optical focal spot within a scattering medium [18].

The first experimental demonstration of optical phase conjugation was performed with stimulated Brillouin scattering in the 1970s [19]. Later on, photorefractive media (with nonlinear susceptibility) were used [2,5,6,10,11]. Because nonlinear media typically have the capacity for high spatial frequency components, OPC based on nonlinear phenomena supports OPC playback over a large collection angle and in a large number of optical modes [1,11]. However, such techniques have practically limited flexibility in terms of working optical wavelength and intensity. More importantly, the OPC reflectivity achievable with such techniques is severely limited and is generally orders of magnitude below unity [20] (see [21]). Moreover, additional manipulation of the phase-conjugated field prior to playback, which is highly preferable in many biomedical applications [22], is not possible with such bulk medium approaches.

To address these limitations in the context of biophotonics applications, an optoelectronic digital OPC system (DOPC) was developed [23,24]. Such a system consists of two parts: a CCD or CMOS camera for wavefront recording and a spatial-light modulator (SLM) for wavefront playback. These two components are precisely aligned around a beamsplitter to optically situate the two digital components in the same optical position. The DOPC procedure follows two steps: (1) the wavefront of the input beam is measured on a sCMOS sensor array using either phase-shifting holography or off-axis holography; and (2) the conjugated copy of the measured wavefront is displayed on an SLM, such as a liquid crystal on silicon (LCoS) or digital micromirror (DMD)-based devices. As the reference beam intensity can be arbitrarily changed, there is no theoretical limit to the maximum OPC reflectivity that can be achieved. Furthermore, such a system allows for further manipulation of the optical wavefront prior to playback. This flexibility is potentially useful and can enable applications such as OPC focal spot scanning [22].

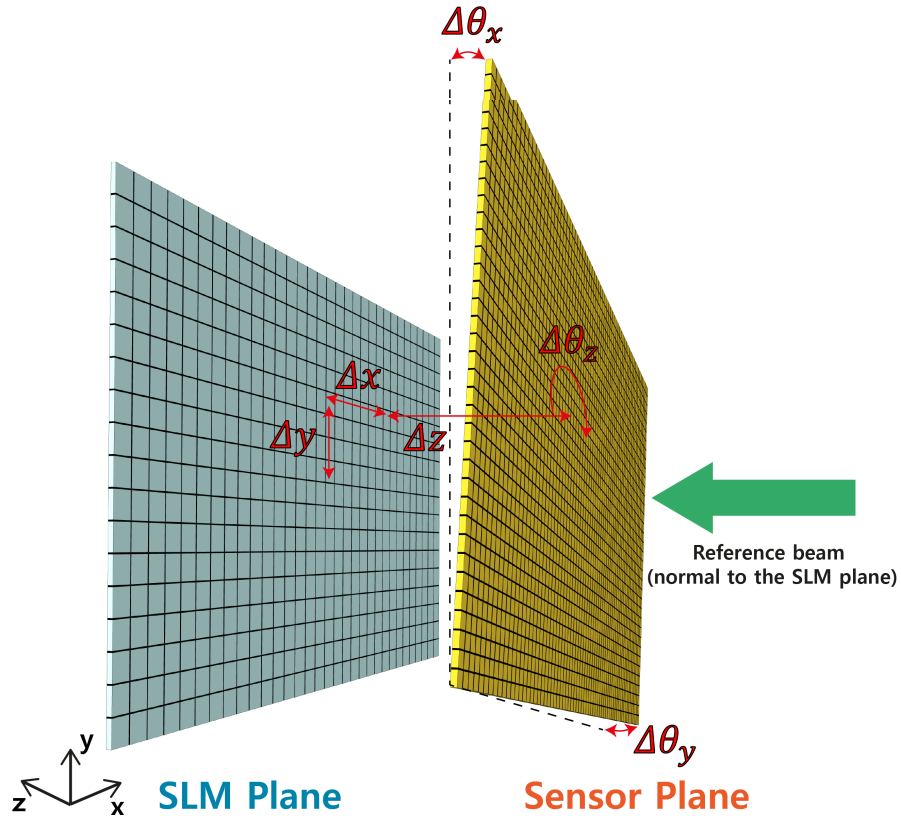


Fig. 1. Six misalignment parameters in the alignment of the sensor plane and SLM plane in three-dimensional space. In-plane translation (Δx and Δy), in-plane rotation ($\Delta\theta_z$), axial translation (Δz), and tip/tilt ($\Delta\theta_x$ and $\Delta\theta_y$) are present. The reference beam is normal to the SLM plane and, thus, it is obliquely incident on the sensor plane.

Despite its significant potential, the practical utility of a DOPC system has been limited by implementation difficulties [23]. In brief, these difficulties stem from the need to achieve pixel-to-pixel matching of the sCMOS sensor array and the SLM in the system. To accomplish pixel-to-pixel matching, the sCMOS sensor array and the SLM need to be finely aligned in six misalignment dimensions: translational (Δx , Δy , and Δz), tip/tilt ($\Delta\theta_x$ and $\Delta\theta_y$), and rotation ($\Delta\theta_z$) (Fig. 1). Previous implementations further require a high quality macro lens to match the pixel size of the sensor and the SLM, if they are originally mismatched. The experimental procedure for bringing the system into precise alignment is highly exact and time-consuming to carry out. To make things worse, the alignment procedure does not allow for a quick ‘shortcut’ realignment of the system if the system drifts out of alignment by even a very small amount (e.g., a few tens of microns). These difficulties are likely to be the major contributive factors that limit the broader application and implementation of DOPC systems beyond a few research groups.

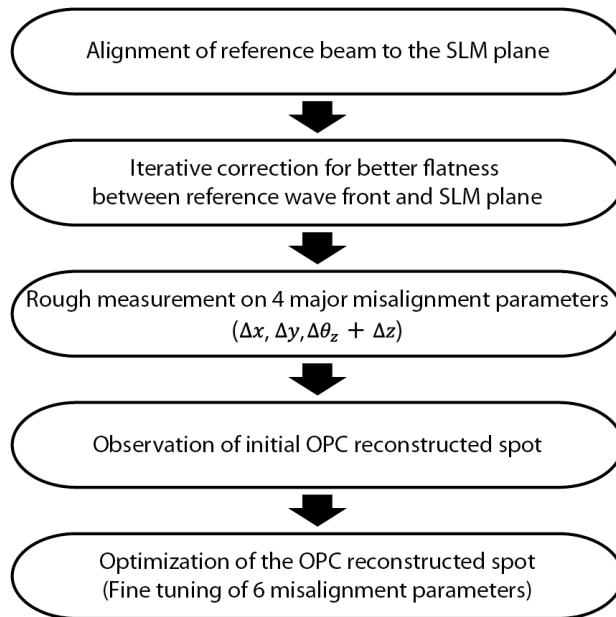


Fig. 2. A scheme of the auto alignment of a DOPC system. Flatness between the reference beam wave front and the SLM plane is optimized by the first two steps. Then, the misalignment parameters (three in-plane parameters Δx , Δy , $\Delta\theta_z$, and axial translation Δz) are roughly measured. Next, the measured incoming wavefront is digitally propagated to the SLM plane with the roughly measured parameters to virtually achieve the rough alignment. At this step, an initial reconstructed DOPC signal (in our case a low contrast focal spot) can be observed. In the last step, all misalignment parameters are finely tuned around the roughly measured parameters while the intensity of the phase-conjugated focal spot (DOPC performance) is optimized.

Here, we report a computational-based alignment strategy for implementing automatic alignment of a DOPC that does not require physically bringing the sCMOS sensor array and the SLM into precise alignment. Instead, this method digitally propagates the optical wavefront as measured at the sCMOS sensor array to the virtual SLM plane. Through this means, optical phase-conjugation playback can be implemented on the SLM even if the measurement plane and SLM plane are not physically aligned. This auto-alignment process is performed through the following steps (Fig. 2). In step 1, a collimated reference beam is directed at the SLM at a normal incidence. A measurement and correction procedure is then performed to correct for reference beam imperfections and SLM curvature (flatness optimization). In step 2, a rough measurement of four major misalignment parameters (Δx , Δy , Δz , and $\Delta\theta_z$) is made. This measurement allows an approximate digital propagation to be performed and allows for the sCMOS sensor array to the SLM to be aligned. This roughly aligned system is then able to render an unoptimized DOPC reconstruction. In step 3, six misalignment parameters are iteratively fine-tuned by monitoring the DOPC reconstruction signal. Through this means, the DOPC system can be brought into optimized virtual alignment. Step 3 can be repeated with ease when mechanical drifts or shocks misalign the DOPC system in minor ways.

This paper is structured as follows. We first describe the experimental setup. Next, we describe the auto-alignment procedure in detail. We then report the experimental validation of this auto-alignment procedure and demonstrate the procedure's capability to recover the virtual alignment in five misalignment scenarios. Finally, we discuss the misalignment

tolerance of the method and its potential limitations. We also discuss the practical significance of the method.

2. Experimental setup and methods

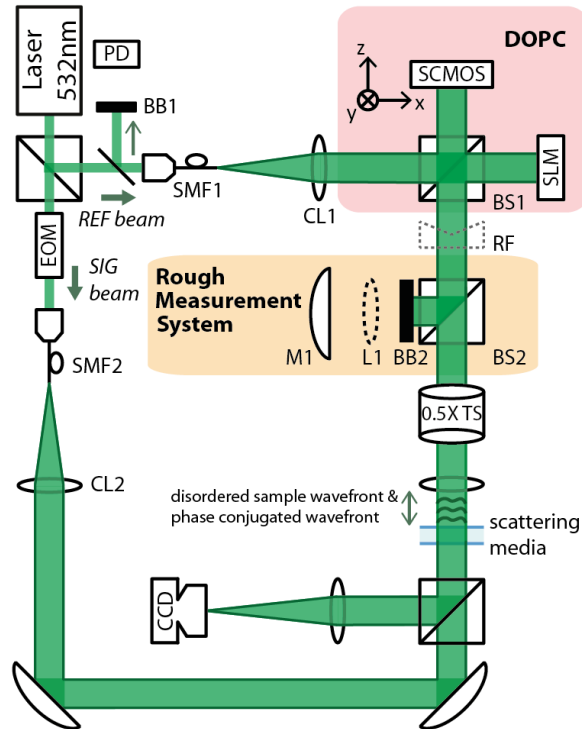


Fig. 3. Experimental scheme of digital OPC. The laser beam is split into two arms: a reference arm and a sample arm. Both arms are spatially filtered by single mode fibers and collimated by plano-convex lens. As the first step of DOPC procedure, the sCMOS camera captures the interferograms created by reference beam and signal beam transmitted through the scattering media (five layers of scattering film). Four-step phase-shifting method is used for the wavefront measurement of the signal beam. EOM, placed on sample arm, shifts the relative phase between two beams. Then, for the time-reversal playback, SLM is used to display the phase-conjugated wavefront, which is measured by the sCMOS camera and digitally propagated. The phase-conjugated light beam (SLM-reflected reference beam) is collimated through the turbid media and creates a focal spot on the CCD camera. Photo diode monitors the back-propagated reference light which is reflected off SLM and propagated back through the single mode fiber (SMF1) for flatness optimization of the reference beam. Microscope cover slip (used due to a high transmission-to-reflection ratio) is placed to sample the back-propagated light. The procedure is detailed in Fig. 4. The Rough Measurement System is used to roughly measure the misalignment between sCMOS camera and SLM in DOPC system. The procedure is described in detail in Fig. 5. Beam blocks stops beam paths to photo diode and the Rough Measurement System during DOPC procedure. SMF, single mode optical fiber; 0.5X TS, 0.5X telescope (from top to bottom); CL, collimation lens; BS, beam splitter; RF, retro reflector; L, lens; M, mirror; BB, beam block; PD, photo diode; EOM, electro-optic phase modulator; SLM, spatial light modulator; sCMOS, scientific CMOS camera; CCD, CCD camera.

Figure 3 shows the experimental setup for our study. The laser beam (532 nm and 150 mW diode-pumped solid state CW) is split into a reference beam and a signal beam. These two beams are spatially filtered by single mode optical fibers (460 HP, Thorlabs) and then collimated. The sample beam, which is scattered by a light-scattering sample (in this case, five layers of scattering film stacked on top of each other, Scotch 810 Magic tape, 3M)

interferes with the reference beam on the sensor plane of the sCMOS camera (pco.edge 5.5, PCO). Phase measurement of the scattering field is then realized by phase-shifting holography (see [25]). An electro-optic phase modulator (EO-PM-NR-C4, Thorlabs) is used to step the relative phase between the reference beam and the sample beam. Then, the phase-conjugated copy of the digitally propagated measured wavefront is displayed on the SLM (PLUTO phase only, Holoeye). The phase-conjugated light beam, which is expected to be collimated after propagating back through the scattering media, is focused on the CCD camera (DMK 31BU03, The Imaging Source). In our system, the pixel dimensions of the sCMOS sensor array and the SLM were 6.5 and 8 microns, respectively, and 2560×2160 and 1920×1080 pixels were present on each device. Thus, the sCMOS sensor array covered a larger area than the SLM. During the experiment, we set the region of interest of the sCMOS sensor array to be 2364×1330 pixels in order to match the physical size of the SLM. Subsystems for optimizing the flatness of the reference beam wavefront to the SLM surface and the rough measurement of misalignment parameters are explained in Sections 2.1 and 2.2.

Throughout this study, the contrast of the phase-conjugated focal spot (peak to background ratio [PBR]) on the CCD was used to quantify the DOPC performance. Here, the peak was the maximum intensity of the DOPC focal spot, and the background was the mean intensity of the speckle pattern on the CCD when a random phase map was displayed on the SLM rather than phase-conjugated copy. By mathematically modeling the scattering medium transmission function as a complex random Gaussian matrix, the PBR can be calculated as $\pi N/4$ where N is the number of optical modes captured/controlled by the DOPC system. Then, N is simply given by P/S where P is the total number of controllable DOPC pixels and S is the speckle coherence area in pixel numbers [26]. If the DOPC system is perfectly aligned, P is given by the smaller value of the number of pixels in the sCMOS sensor array and the SLM (in our case, 1920×1080 since the SLM has a smaller number of pixels). In our experiment, speckle granularity was around 3×3 SLM pixels. Thus, the theoretical maximum PBR was 180000.

2.1. Flatness optimization of the reference wavefront to the SLM surface

The optimal performance of the DOPC system requires that the reference beam's wavefront be fully characterized on both the sCMOS sensor array and the SLM surface. This is because the reference beam serves both as the interfering reference beam for wavefront measurement of the incoming signal light field on the sCMOS sensor array and as the 'blank' input wavefront that the SLM subsequently modifies to create the OPC field. In the conventional DOPC system, we would exactly align a collimated reference beam normal to the SLM and precisely align the sCMOS sensor array to the SLM at the individual pixel level [23]. The collimation and normal incidence condition simplified the DOPC processing as we were able to accomplish DOPC playback by simply projecting a sign-reversed copy of the measured phase variations from the sCMOS sensor array onto the SLM [23]. In practice, however, available SLMs have considerably curved surfaces and reference beams cannot be assumed to be perfectly flat.

To address these limitations, we compensated for marginal imperfections in the reference wavefront and SLM surface curvature (deviation from perfect flatness) by finding the SLM phase pattern that transforms the reference beam to be flat in phase spatially during reflection [15]. This typically boosted the OPC performance by 2-5 times (depending on the initial alignment between the reference beam and the SLM plane).

This procedure was accomplished by going through the following steps. First, as is done in the conventional DOPC system, a retroreflector (RF) was temporarily inserted into the setup (gray dotted line, see Fig. 3) to create a Michelson interferometer. This allowed us to make the reference beam (directed onto the sCMOS sensor array by the beamsplitter) interfere with the SLM-reflected reference beam (directed onto the sCMOS sensor array by

the beamsplitter, BS1 in Fig. 3, and retroreflector, RF (gray dotted line) in Fig. 3). We then tip/tilt the SLM or adjust incidence angle of reference beam to SLM until the dominant lowest spatial frequency component of the observed interference pattern was at its lowest possible value. If the reference wavefront and SLM plane were flat, the interference pattern would be completely uniform when the normal incidence is achieved. However, as there were practical imperfections, we ensured that the reference beam was almost normal to the SLM by observing for the pattern with lowest possible frequency. This step minimizes the marginal imperfections we need to correct in the next step.

We next proceeded to determine an appropriate compensation phase pattern to display on the SLM that would ensure that the reflected reference beam was spatially flat in phase. This was done by observing the collected power at the photo diode (PD) (2001-FS, New Focus) in Fig. 3. A simplified vignette of the experimental scheme that is relevant for this process is shown in Fig. 4. In brief, the reference light reflecting off the SLM propagates back through the SLM and is in turn detected by the PD. This signal is maximized if the reflected reference beam is spatially flat in phase. As shown in Fig. 3, the reference beam is spatially filtered by SMF 1 and collimated by collimation lens CL 1. Then, the reference beam is reflected off the SLM and focused back on the SMF 1 through CL1. Therefore, if the optical flatness between the reference wavefront and SLM surface is retained by displaying a compensation phase pattern, SLM-reflected light couples back to the SMF 1 with high efficiency.

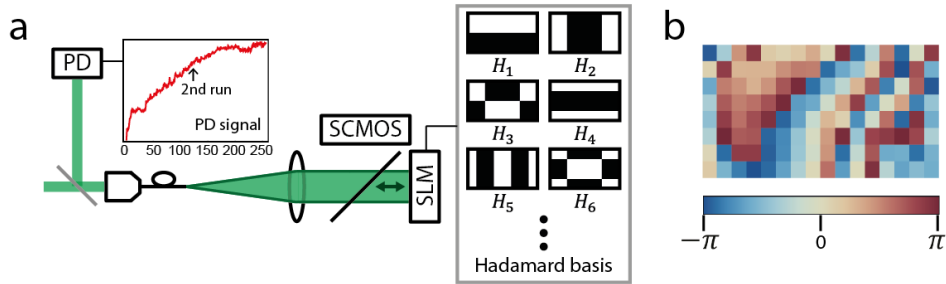


Fig. 4. Iterative searching for an SLM pattern assuring flatness of the reference wavefront to the SLM surface. (a) SLM iteratively displays the phase map that consists of the optimized phase map from the previous step and the “+1” part of a Hadamard pattern (H_n). For each iteration, four measurements from the PD were obtained by stepping in phase on a Hadamard basis by $\pi/2$. An optimized phase map based the Hadamard basis was calculated using these four measurements. The PD signal inset shows the photo diode signal optimized during the iterative procedure. The Hadamard basis inset shows the 2D discrete Hadamard basis used for each iteration step (with the “+1” part in white and “-1” part in black). (b) Acquired phase map after two runs of the iterative procedure. This map optimizes the flatness between the reference wavefront and the SLM surface.

In our experiment, we iteratively searched the phase map to maximize the PD signal (optimizing flatness). Here, we used the 16×8 Hadamard basis (1920×1080 SLM pixels divided into 128 sections of $120 \text{ pixels} \times 135 \text{ pixels}$) as the input basis [27]. That is, starting from the pattern with low spatial frequency, the optimum phase (ϕ_n) for the “+1” part of each Hadamard pattern (H_n , Fig. 4 Hadamard basis inset) was obtained. This choice of basis was very suitable for this purpose because the optical aberration and the SLM curvature were mainly in the low spatial frequency regime. Also, as half of the SLM pixels were modulated, the signal-to-noise ratio (SNR) at the PD was largely improved compared to the SNR of pixelwise optimization [27].

The iteration procedure was as follows. The n^{th} phase pattern displayed on the SLM (ψ_n) consisted of two components – the optimized phase pattern from the previous iteration (ψ_{n-1})

and the “+1” part of the Hadamard basis (H_n , shown in Fig. 3 inset, “-1” part with zero phase). While displaying the addition of two phase maps, we stepped the phase of the “+1” part (white portion in the inset) in four phases (e^{iH_n} , $e^{i(\pi/2)H_n}$, $e^{i\pi H_n}$, and $e^{i(3\pi/2)H_n}$). Consequently, the four interference intensity ($I_{n,1}$, $I_{n,2}$, $I_{n,3}$, and $I_{n,4}$) were measured from the PD. Mathematically, the interference intensity was $I_{n,k} = |E_{\text{mod}}e^{ik\pi/2} + E_{\text{unmod}}|^2$ where E_{mod} and E_{unmod} were resultant fields at the PD from modulated pixels and unmodulated pixels of the SLM, respectively. Then, the optimized phase for the n^{th} Hadamard basis was simply calculated as $\phi_n = \tan^{-1}[(I_{n,2} - I_{n,4})/(I_{n,1} - I_{n,3})]$. The optimized phase pattern (ψ_n) was then updated by adding the Hadamard basis with the optimized phase ($\psi_{n-1} + H_n\phi_n$). As shown in the Fig. 4(a) PD signal inset, the PD signal increases as the flatness is compensated at each iteration step. After 128 iteration steps for each Hadamard basis, the phase map optimizing the flatness between the reference wavefront and the SLM was obtained (ψ_{128}). The flatness can be further improved by repeating this iterative loop based on the optimized phase map from the previous run. In our experiment, we ran the iterative loop twice. At the end, when we played back the OPC beam, and the optimized pattern from the second run (shown in Fig. 4(b)) was added to the phase-conjugated wavefront.

2.2. Rough measurement of the major misalignment parameters Δx , Δy , Δz , and $\Delta\theta_z$

DOPC alignment can be viewed as an optimization procedure with a global maximum (corresponding to the alignment with the highest DOPC PBR). The simplest strategy for finding the maximum would be an exhaustive parameter search. However, due to the number of parameters, this strategy would be slow and inefficient, particularly when starting far from the maximum. We, therefore, adopted a strategy in which we first obtained rough estimates of the misalignment parameters, in order to get closer to the maximum. Only then were parameters fine-tuned by a search strategy.

Rough measurements were done in two steps – measurement of in-plane misalignment parameters (Δx , Δy , and $\Delta\theta_z$) and measurement of axial displacement (Δz). A subsystem for the rough measurement simply consisted of a plane mirror and a bulk lens (focal length 7.5 cm). As done for the SLM, the mirror surface was also aligned perpendicular to the incoming reference beam. The detailed procedure for the measurement is described in Sections 2.2.1 and 2.2.2.

Before proceeding, we would like to note that the tip/tilt misalignment of the sample and reference beams relative to the sCMOS sensor array does not actually have a significant impact on the DOPC performance. This robustness at the detection side is in remarkable contrast to the exacting alignment by which we ensure that the reference beam is normal to the SLM. This can be explained by noting that tip/tilt misalignment of the reference beam to SLM plane would result in a subsequent DOPC playback that is angled off from its intended path. In contrast, the sCMOS would still be able to obtain a reasonably accurate measurement of the interference light field if the tip/tilt of the sCMOS is small.

To clearly illustrate this point, consider the interference of a sample beam with a reference beams that subtends an angle of θ_{sam} . Further suppose that the reference beam is at an angle of $\Delta\theta_{x \text{ or } y}$ with respect to the sCMOS sensor array ($\Delta\theta_{x \text{ or } y} = 0$ would mean that the reference beam is at normal incidence). The resulting interference fringe pattern we would see would have a periodicity given by:

$$k \sin(\theta_{\text{sam}} - \Delta\theta_{x \text{ or } y}) - k \sin(-\Delta\theta_{x \text{ or } y}) \approx k \sin(\theta_{\text{sam}}) \quad (1)$$

when θ_{sam} and $\Delta\theta_{x\text{ or }y}$ are both small. k is the wave number. Notice that the $\Delta\theta_{x\text{ or }y}$ has no contributive component in the simplification of the equation. In other words, as long as θ_{sam} and $\Delta\theta_{x\text{ or }y}$ are both small, the sCMOS sensor would see the same interference pattern that is independent of the tip/tilt misalignment. In most DOPC system, the range of θ_{sam} we work with is actually quite small (a span of $\sim 6^\circ$ is typical). As such, we can ignore tip/tilt misalignment as long as the misalignment is small (within the range of 10° or less) as well.

2.2.1. Rough measurement on in-plane misalignment parameters (Δx , Δy , and $\Delta\theta_z$)

For in-plane misalignment parameters (Δx , Δy , and $\Delta\theta_z$), four Fresnel zone patterns were displayed on the SLM, which is equivalent to four convex lenses (Fig. 5(b)). The focal length of these Fresnel zone pattern was chosen so that four focal spots were projected onto the sensor plane (Fig. 5(c)). The reference beam is reflected off the SLM plane and relayed by BS1, BS2, M1, BS2, and BS1 in the order as shown in Fig. 5(a). Δx and Δy were then be simply estimated by measuring the distances between the positions of measured four points (magenta points in Fig. 5(c)) and the ideal positions of the points (center of the zone plates, white points in Fig. 5(c)). For the rotation ($\Delta\theta_z$), the angle between the horizontal line and the line connecting the two bottom points or two top points was evaluated. When the tip/tilt misalignment ($\Delta\theta_x$ and $\Delta\theta_y$) was large, we also roughly measured these parameters from the four spots by observing the extended distance between the spots.

2.2.2. Rough measurement on axial displacement misalignment (Δz)

In order to measure the axial displacement (Δz), a plano-convex lens (7.5 cm focal length) was placed between the SLM and the mirror (Fig. 2). In this case, only a single Fresnel zone pattern was displayed on the SLM (Fig. 5(e)). The focal length of this zone pattern was chosen such that the SLM-reflected light beam focused on the focal plane of the lens (L1) which collimated the beam. This beam was then reflected off the mirror (M1) and focused back on the plane on which the original focal spot was made (Fig. 5(d)). The interference between the original reference beam (reflected off the BS1) and the beam that travels through the rough measurement system created an interference pattern (Fresnel zone pattern) on the sensor plane. Then, the focal length of the measured Fresnel zone pattern was obtained by fitting it to a lens transmission function ($= e^{ik(x^2+y^2)/2f}$, here f is the focal length). Finally, we roughly determined the axial displacement between two planes by comparing the fitted focal length of the measured zone pattern on the sensor (Fig. 5(f)) and the focal length of the original zone pattern displayed on the SLM (Fig. 5(e)).

We could roughly achieve the virtual alignment by plugging the roughly measured parameters (Δx , Δy , $\Delta\theta_z$, and Δz) into the digital light propagator. This allowed us to render an unoptimized OPC focal spot that served as the feedback source for the parameter fine-tune procedure.

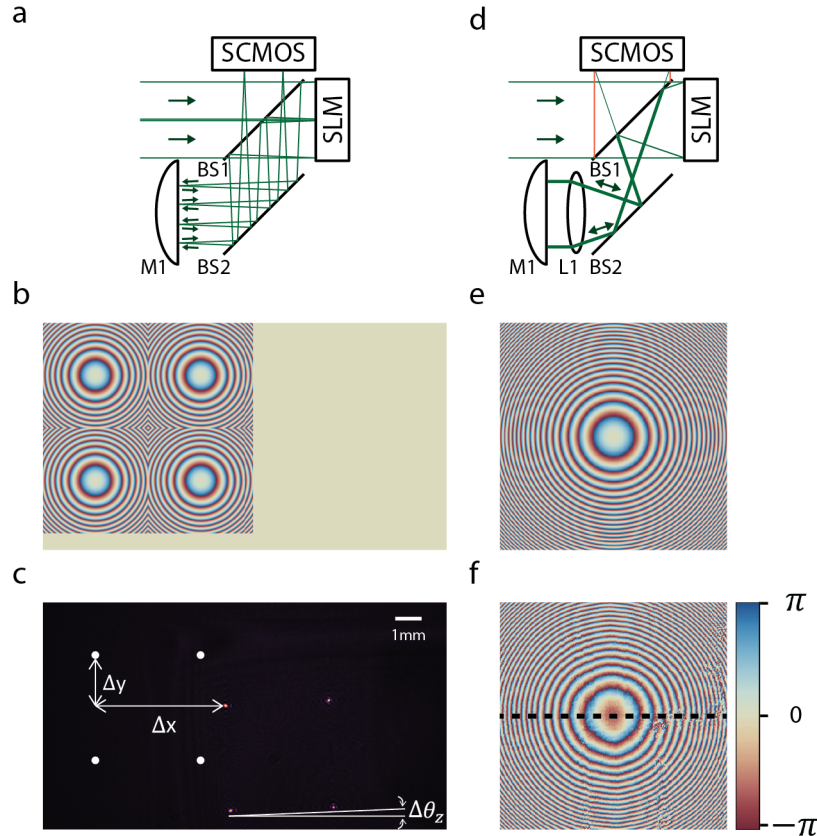


Fig. 5. Rough measurement of the four major misalignment parameters. (a, b and c) Measurement of in-plane misalignment parameters. (a) Four Fresnel zone patterns are displayed on the SLM so that the mirror-reflected light creates four foci on the sCMOS sensor plane (two are shown here assuming the top view). (b) Four Fresnel zone patterns displayed on the SLM for the measurement of in-plane misalignment parameters. (c) Four foci created on the sCMOS sensor plane (magenta points). The overlaid white points are the ideal position of the four foci that the precisely aligned system is supposed to create. Δx and Δy are roughly measured by comparing the distances between the ideal spots and measured spots. $\Delta\theta_z$ is simply estimated by the angle between the horizontal line and the line connecting the bottom left point and the bottom right point (or the upper left point and the upper right point). (d, e, and f) Measurement of the axial displacement. (d) The single zone pattern is displayed. The lens is placed in between the mirror and the SLM so that the focused light is collimated, reflected off the mirror, and focused back on to the same plane with the original focal spot. Then, using the phase-stepping method, the wavefront of the back-propagated light into the sCMOS (by the interference between the red and green light rays) is measured. (e) The zone pattern displayed on the SLM for the measurement of the axial displacement. (f) The zone pattern measured from the sCMOS camera. By comparing the corresponding focal length of the displayed and the measured zone patterns (the focal length of the measured zone pattern is determined by fitted the measured profile along the dotted line to a 1D lens transmission function), the axial translation (Δz) is determined.

2.3. Digital light propagation

The digital propagator is implemented with a scalar diffraction theory based on the angular spectrum method [28–30] (as shown in Fig. 6). In contrast to the other scalar diffraction theories such as the Fresnel diffraction formula and the Kirchhoff diffraction formula, the angular spectrum method provides the diffraction field without approximation. Here, it was performed in three steps: (1) decomposition of the measured field (Fourier transform) into

Fourier components (the measured field is shown in Fig. 6 upper left); (2) propagation (adding phase corresponding to the axial misalignment) of each Fourier components (Fig. 6 bottom); and (3) addition of the Fourier components (inverse Fourier transform) at the reference plane (inverse Fourier transformed field is shown in Fig. 6 upper right), here the SLM plane. Assuming f_x and f_y are spatial frequencies defined on the SLM plane, the angular spectrum method is mathematically expressed as

$$U_{SLM}(x, y) = \int_{f_x, f_y} \hat{U}_{SA}(f_x, f_y) H_{AS}(f_x, f_y) \exp(-2\pi i f_x x) \exp(-2\pi i f_y y) df_x df_y \quad (2)$$

where \hat{U}_{SA} and H_{AS} are Fourier components of the measured field and the angular spectrum transfer function. U_{SLM} is the propagated field on the SLM plane. H_{AS} is given as

$$H_{AS}(f_x, f_y) = \exp\left[ik\Delta z \sqrt{1 - (\lambda f_x)^2 - (\lambda f_y)^2}\right] \quad (3)$$

where λ is the wavelength so that the exponential term is simply the additional phase of the Fourier component at (f_x, f_y) as it propagates for Δz .

The formula above is based on the regular angular spectrum diffraction theory describing diffraction of the light field between two parallel planes. To take account of the fact that the sensor plane is tip/tilted with respect to the SLM plane by $\Delta\theta_x$ and $\Delta\theta_y$, we first added the phase gradient of the oblique reference wave on the measured wavefront. Because the reference beam is normally incident on the SLM plane, it arrived on the sCMOS sensor array with an oblique angle of $\Delta\theta_x$ and $\Delta\theta_y$, as shown in Fig. 1. Then, we considered the transformation to relate the Fourier basis of the measured plane (f'_x, f'_y , \hat{U}_{SA} is initially calculated) into the Fourier basis of the SLM plane (f_x, f_y) using the following rotation [30]:

$$(f_x, f_y, f_z(f_x, f_y)) = T(f'_x, f'_y, f'_z(f'_x, f'_y)) \quad (4)$$

where T is a transformation matrix given by $T = R_x^{-1} R_y^{-1}$ ($T^{-1} = R_y R_x$). R_x and R_y are rotation matrices along the x and y axes, respectively. They are given by

$$R_x = \begin{bmatrix} 1 & 0 & 0 \\ 0 & \cos(\Delta\theta_x) & -\sin(\Delta\theta_x) \\ 0 & \sin(\Delta\theta_x) & \cos(\Delta\theta_x) \end{bmatrix} \quad \text{and} \quad R_y = \begin{bmatrix} \cos(\Delta\theta_y) & 0 & \sin(\Delta\theta_y) \\ 0 & 1 & 0 \\ -\sin(\Delta\theta_y) & 0 & \cos(\Delta\theta_y) \end{bmatrix}. \quad (5)$$

This transformation allowed us to express the Fourier components of the measured wavefront on the sCMOS sensor array on the Fourier basis of the SLM plane.

We corrected the in-plane displacement misalignment by using the following functional relationship for shifting:

$$U_{SLM}(x - \Delta x, y - \Delta y) \leftrightarrow \exp(-2\pi i \Delta x f_x) \exp(-2\pi i \Delta y f_y) \hat{U}_{SLM}(f_x, f_y). \quad (6)$$

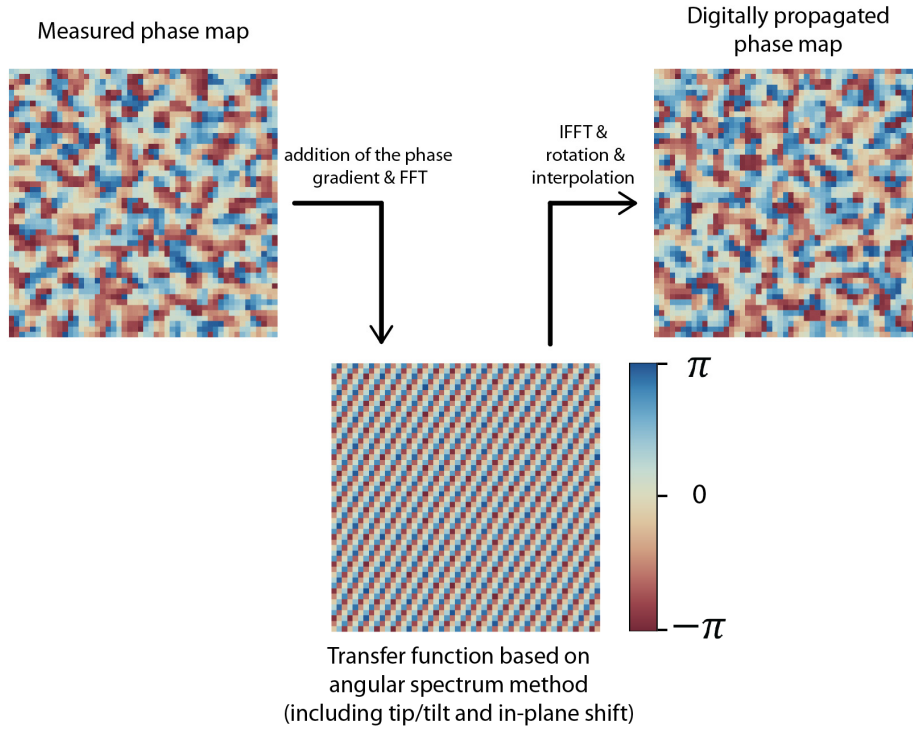


Fig. 6. Auto-alignment based on digital propagation with an angular spectrum method. First, the measured phase map from the sCMOS sensor array is multiplied with the phase gradient of the oblique reference beam (corresponding to $\Delta\theta_x$ and $\Delta\theta_y$) and Fourier transformed. Then, the Fourier components are multiplied with the transfer function based on the angular spectrum method (including tip/tilt and in-plane shifts). Thus, the five misalignment parameters (Δx , Δy , Δz , $\Delta\theta_x$, and $\Delta\theta_y$) are taken account in this step. Then, the map in the Fourier domain is the inverse Fourier transformed to get the phase map on the SLM plane. At the final step, the phase map is rotated ($\Delta\theta_z$) and interpolated at each SLM pixel position.

Finally, the digital propagation of the measured field correcting all of the misalignment except the in-plane rotation (θ_z) was given by

$$U_{SLM}(x, y) = \int_{f_x, f_y} \hat{U}_{SA}^{tip/tilt}(T^{-1}(f_x, f_y, f_z(f_x, f_y))) H_{AS}(f_x, f_y) |J(f_x, f_y, f_z(f_x, f_y))| \times \exp(-2\pi i f_x(x + \Delta x)) \exp(-2\pi i f_y(y + \Delta y)) df_x df_y \quad (7)$$

where $\hat{U}_{SA}^{tip/tilt}$ is the Fourier component (expressed with the basis on the SLM plane with T^{-1}) of the measured field multiplied by the phase gradient due to the tip/tilt of the sensor plane. That is, in the spatial domain, $U_{SA}^{tip/tilt}(x', y')$ is $U_{SA}(x', y') \exp(i(kT_{1,3}^{-1}x' + kT_{2,3}^{-1}y'))$ x' and y' are the axes defined on the sensor plane. $J(f_x, f_y, f_z(f_x, f_y))$ is the Jacobian determinant to correct the energy factor ($\propto |\hat{U}_{SA}|^2$) along (df_x, df_y) as the transformation T is nonlinear. It is given by

$$J(f_x, f_y, f_z(f_x, f_y)) = (T_{1,2}^{-1}T_{2,3}^{-1} - T_{1,3}^{-1}T_{2,2}^{-1}) \frac{f_x}{f_z(f_x, f_y)} + (T_{1,3}^{-1}T_{2,1}^{-1} - T_{1,1}^{-1}T_{2,3}^{-1}) \frac{f_y}{f_z(f_x, f_y)} + (T_{1,1}^{-1}T_{2,2}^{-1} - T_{1,2}^{-1}T_{2,1}^{-1}) \quad (8)$$

At the end, U_{SLM} is rotated by the angle $\Delta\theta_z$ and interpolated at the positions of each sensor pixel.

2.3.1. Fine tuning of the parameters

As mentioned above, the initial OPC peak was observed by displaying the phase-conjugated copy of the propagated field with roughly measured parameters. However, in most cases, the OPC peak-to-background ratio is much lower than the theoretical value due to the limited accuracy by which the misalignment parameter can be measured. Thus, we fine-tuned the parameters to further improve the system performance. This was done by scanning over the parameter spaces around the roughly measured parameter set while optimizing for the intensity of the phase-conjugated focal spot. We scanned parameters in the order of Δx , Δy , Δz (displacement), $\Delta\theta_z$ (in-plane rotation), $\Delta\theta_x$, and $\Delta\theta_y$ (tip/tilt) and repeated this sequence with a smaller step size until the maximized OPC peak intensity was converged. Step sizes are empirically chosen based on the speckle size of the measured wavefront. Typically, it takes around 10 minutes to find optimal parameters. It is expected to be shortened with a fast detector (e.g. photodiode) for measuring OPC peak intensity and a better algorithm to search the optimized parameters.

3. Results

In this section, we present the results we acquired while recovering the DOPC performance from a highly misaligned system (in all 6 parameters) as a case study: the (1) images we captured for the rough measurement of the misalignment parameters, (2) measured misalignment parameters, (3) OPC reconstructed spot with the roughly measured parameters, (4) fine-tuned misalignment parameters, (5) optimized misalignment parameters, and (6) OPC reconstructed spot with the optimized parameters. And, in the subsequent section, we present the table of misalignment parameters (measured and optimized) and the corresponding PBR for five different misaligned scenarios.

3.1. Auto-alignment of a DOPC system

For demonstration purposes, we misaligned the sCMOS sensor array and the SLM in six degrees of freedom associated with all six misalignment parameters using translational, rotation, and tip/tilt stages. The in-plane translation misalignment was in the order of a millimeter, and the axial translation misalignment was in the order of a centimeter. For the rotation and tip/tilt, several degrees of misalignment were applied.

Figure 5(c) shows the four spots on the sCMOS sensor array (created by zone plates on the SLM as described in section 2.2.1). From this image, we estimated Δx , Δy , and $\Delta\theta_z$ by $-5006 \mu m$, $-1845 \mu m$, and -2.39° using the rough measurement method described in section 2.2.1. For the axial misalignment, as mentioned in section 2.2.2, we compared two focal lengths fitted one from the measured zone plate on the sCMOS sensor array (Fig. 5(f)) and displayed one on the SLMs (Fig. 5(e)). We determined the axial misalignment to be $17514 \mu m$.

Then, we plugged those roughly measured parameters into the digital propagator and observed an OPC reconstructed spot, albeit with comparably low PBR of 60 (Fig. 8(b)). The roughly measured parameters were subsequently used as a basis for iterative fine tuning.

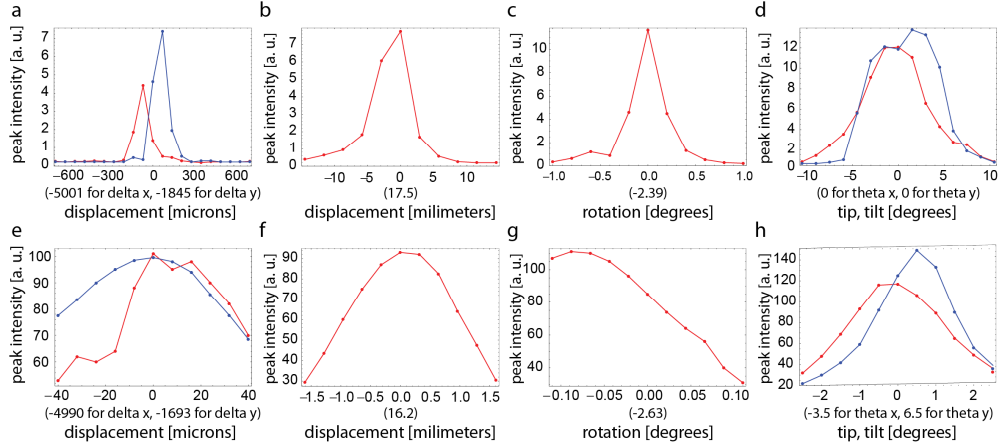


Fig. 7. Optimization of the OPC reconstructed spot during the fine-tuning of the misalignment parameters. The peak intensities were measured from the CCD camera while scanning one parameter at a time. (a) and (e) for Δx (red) and Δy (blue). (b) and (f) for Δz . (c) and (g) for $\Delta\theta_z$. (d) and (h) for $\Delta\theta_x$ (red) and $\Delta\theta_y$ (blue). The upper row shows the signals measured during the rough scanning at the beginning of the fine-tune procedure. The bottom row shows the signals measured during the fine scanning at the end of the fine-tune procedure.

As described above, the fine optimization of the parameters was started from the most significant parameters, Δx and Δy , then Δz , $\Delta\theta_z$, $\Delta\theta_x$, and $\Delta\theta_y$ in the order of decreasing significance. At each scanning step, the misalignment parameters were plugged into the digital propagator for correction. Then, the corresponding OPC peak intensity of the focal spot was measured. As an example, Fig. 7 shows the measured peak intensity while we were scanning through each misalignment parameters. For an effective search of optimized parameters, we first scanned the parameters with a large step size and then repeated the scan with a smaller step size. In Fig. 7, upper row and lower row present the DOPC focal spot intensity during scanning with a large step size and a small step size, respectively. The optimized parameters were found to be $-4990 \mu\text{m}$, $-1693 \mu\text{m}$, $16231 \mu\text{m}$, -3.5° , -7.0° , and -2.72° (for Δx , Δy , Δz , $\Delta\theta_z$, $\Delta\theta_x$, and $\Delta\theta_y$). So, the error of the rough measurement was $16 \mu\text{m}$, $152 \mu\text{m}$, and -0.33° (for Δx , Δy , and $\Delta\theta_z$) and $-1283 \mu\text{m}$ (for Δz).

At last, the virtually aligned DOPC performance was demonstrated by comparing the PBR without correction, with rough correction alone (digital propagation with roughly measured parameters), and with fine correction (digital propagation with fine-tuned parameters). As shown in Fig. 8(a), no focal spot was observed on the CCD camera without correction. After rough correction, the PBR of OPC focal spot was ~ 60 (Fig. 8(b)) and it increased to ~ 52000 after fine tuning for PBR maximization. The measured field at the sCMOS sensor array ($U_{SA}(x', y')$), transfer function including tip/tilting and displacement ($H_{AS}(f_x, f_y) |J(f_x, f_y, f_z(f_x, f_y))| \times \exp(-2\pi i f_x \Delta x) \exp(-2\pi i f_y \Delta y)$), and correspondingly digitally propagated and rotated (by $\Delta\theta_z$) field ($U_{SLM}(x, y)$) are presented in Fig. 6.

Here, the DOPC PBR was enhanced by ~ 870 times compared to that of the DOPC system corrected only with roughly measured parameters. The achieved PBR was about 30% of the theoretical PBR limit. This PBR performance is rarely achieved in manually aligned DOPC systems.

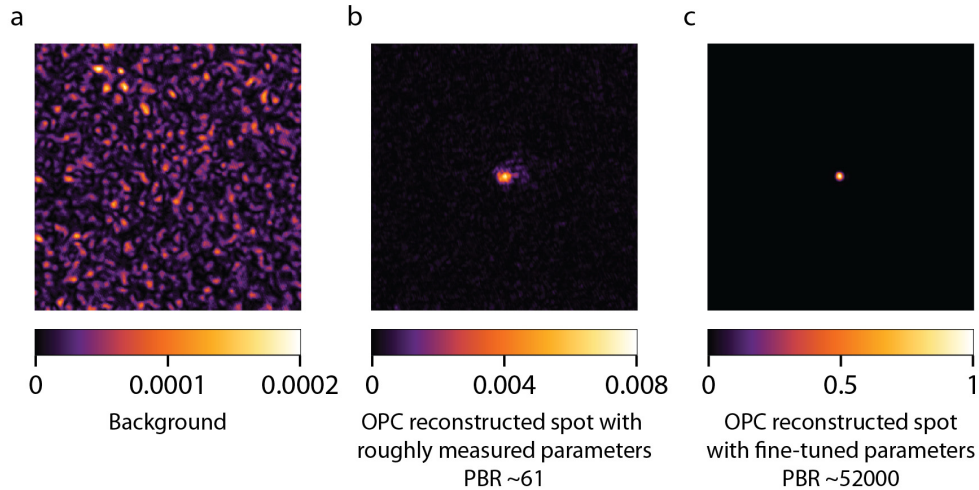


Fig. 8. (a) Background and (b) DOPC reconstructed spot with roughly measured parameters and (c) optimized parameters (normalized by the optimized peak intensity with the fine-tuned parameter). (a) Without optimization, we observed only background as the misalignment significantly deteriorated the DOPC system. (b) With roughly measured parameters, the OPC peak was observed with low quality (PBR ~ 61). (c) With fine-tuned parameters, the peak intensity was 870 times increased. A PBR of ~ 52000 was observed, which corresponds to ~ 0.31 of the ideal PBR.

3.2. Case studies

Table 1. Five case studies. An auto-alignment scheme was applied to five different misaligned configurations of the sCMOS sensor array and SLM. The values in between parentheses in the “Fine-tuned parameters” column are the differences between the roughly measured parameters and fine-tuned parameters. Thus, they present the accuracy of measurement on the four measured parameters. The values in between parentheses in the “Optimized PBR” column are the ratio of optimized PBR to the theoretical maximum, 180000. Misalignment parameters are in units of μm and degrees. As the control set, the result from a roughly aligned system is presented.

Set	Roughly measured parameters ($\Delta x, \Delta y, \Delta z, \Delta\theta_x, \Delta\theta_y, \Delta\theta_z$)	Initial PBR	Fine-tuned parameters ($\Delta x, \Delta y, \Delta z, \Delta\theta_x, \Delta\theta_y, \Delta\theta_z$)	Optimized PBR
1	-5006, -1845, 17514, 0, 0, -2.39	60	-4990, -1693, 16231, -3.5, 7, -2.72 (16, 152, -1283, -3.5, 7, -0.33)	52000 (29%)
2	-2606, -2233, 8416, 0, 0, -2.87	1500	-2590, -2041, 9057, 0.5, 0.5, -2.82 (16, 192, 642, 0.5, 0.5, 0.05)	82000 (45%)
3	-2541, -2197, 3186, 0, 0, -2.85	1300	-2517, -2029, 3828, 1, -1, -2.83 (24, 168, 642, 1, -1, 0.02)	85000 (47%)
4	-177, -1315, 10801, 0, 0, -1.96	23000	-217, -1315, 11122, 1, 0, -1.8 (-40, 0, 321, 1, 0, 0.16)	97000 (53%)
5	284, -1306, 2528, 0, 0, -2.10	3600	260, -1314, 1887, 1, 2, -1.76 (-24, -8, -642, 1, 2, 0.33)	100000 (55%)
Control (PBR ~ 5400 w/o any correction)	22, -34, 2773, 0, 0, -0.69	170	24, -40, 3850, -0.5, -2.5, -0.09 (2, -6, 1077, -0.5, -2.5, 0.60)	120000 (66%)

In this section, we examine the performance of our auto-alignment strategy for several scenarios (including the one already presented as Set 1 in Table 1). Table 1 presents the roughly measured parameters, corresponding PBR, optimized parameters, and optimized PBR

for each misaligned scenario. We have repeatedly and successfully achieved an optical phase conjugation procedure. For all configurations, PBR was recovered to more than 50000 ($\sim 30\%$ of the theoretical maximum).

The Control set in the table shows the results we obtained while correcting a roughly aligned system (physically roughly aligned based on the roughly measured parameters). We applied our technique to the physically roughly aligned DOPC system to experimentally investigate the optimal DOPC performance which would be practically beneficial for the optimal performance of various applications, as such for the contrast of high-resolution imaging. The absolute PBR of ~ 120000 was achieved, corresponding to $\sim 66\%$ of the theoretical maximum.

Empirically, precision of the rough measurement was in the order of $\sim 100\mu m$ for Δx and Δy , $\sim 0.5^\circ$ for $\Delta\theta_z$, and $\sim 1000\mu m$ for Δz . In the case studies, even though the speckle coherence area was around $24\mu m \times 24\mu m$ (3×3 SLM pixels), the rough measurement was sufficiently accurate to allow the initial reconstructed peak to be observed because of the memory effect of the thin scattering sample [31]. For the thick turbid media, this precision might not be good enough to render the initial reconstructed peak. However, this challenge can be simply circumvented by digitally filtering out the high spatial frequency components of the measured field. This enables the observation of the initial reconstructed peak with the correction based on the roughly measured parameters. Thus, the fine-tuning of the misalignment parameters can be applied. This process can then be repeated with the higher spatial frequency part of the measured wavefront until PBR is maximized.

4. Discussion

DOPC is a novel and promising technique for turbidity suppression in biomedical imaging, but the requirement for precise system alignment poses significant challenges to its practical implementation. As our data show, even small misalignments, particularly lateral shifts and in-plane rotations between the camera and the SLM, can lead to drastic reductions in DOPC performance. Here, we introduced a versatile easy-to-use method that significantly reduces the effort and time required for precise alignment. Even with untypically large misalignments of several millimeters for displacement and several degrees for rotation and tip/tilt, our method converges to optimal performance within 10 minutes. For small scale misalignments (less than a hundred μm and one degree), our fine tuning method can be completed within three minutes, which is well-suited for drift correction on a daily basis. Our system has robustly achieved optical phase conjugation with a high fidelity (PBR of 52000–120000, corresponding to 29%–66% of the theoretically achievable PBR of ~ 180000), which is comparable to that of conventional precision alignment.

It should be noted that the PBR is typically below 100% of the ideal PBR ($= \pi N/4, 180000$) even with the exact pixel-to-pixel physical/virtual matching alignment because of the following reasons: (1) There is a crosstalk between SLM pixels so that the phase of the phase-conjugated field cannot be precisely addressed. This effect becomes more significant when the phase pattern contains high spatial frequency components such as the fine speckle in our experiments (speckle granularity was around 3×3 SLM pixels). (2) Digital components such as sCMOS sensor array and SLM are pixelated. Thus, we cannot capture/display all nuances of the incoming/phase-conjugated field.

We note that some loss in PBR is always to be expected for physically misaligned systems, even with optimal correction by our auto-alignment technique. Because our method is based on the digital light propagation of optical wavefronts from the sensor plane to the SLM plane, a portion of the digitally propagated wavefront may fall outside of the virtual SLM plane (loss in information) such that the entire measured field at sensor plane is not reproducible by the SLM. This explains the gradual drops in PBR (equivalent to the gradual

drops in the effective number of DOPC pixels, P) in our experimental results as the misalignment become severe.

While such hardware limitations reduce the number of effectively controlled modes, our routinely achieved PBR of over 50000 would still provide a sufficient contrast for high resolution imaging. Furthermore, ongoing improvement of SLM hardware by the industry is likely to reduce cross-talk and increase the number of SLM pixels in the near future, which will lead to a further increase in DOPC performance.

With such hardware advances and the considerable reduction in alignment complexity and time presented in this paper, we expect that our new alignment strategy will aid the dissemination of DOPC in the field of biomedical optics.

Acknowledgments.

We thank Mr. Roarke Horstmeyer for helpful discussions. This work was supported by NIH 1DP2OD007307-01. Benjamin Judkewitz is a recipient of a Sir Henry Wellcome Fellowship from the Wellcome Trust.